

The warm, the excited, and the molecular gas: GRB 121024A shining through its star-forming galaxy. *

M. Friis¹, A. De Cia², T. Krühler^{3,4}, J. P. U. Fynbo⁴, C. Ledoux³, P. M. Vreeswijk²,
D. Malesani⁴, J. Gorosabel^{5,6,7}, R. L. C. Starling⁸, P. Jakobsson¹, K. Varela⁹,
D. J. Watson⁴, K. Wiersema⁸, A. P. Drachmann⁴, A. Trotter^{10,11}, C. C. Thöne⁵,
A. de Ugarte Postigo^{5,4}, V. D’Elia^{12,13}, J. Elliott⁹, M. Maturi¹⁴, P. Goldoni¹⁵,
J. Greiner⁹, J. Haislip¹⁰, L. Kaper¹⁶, F. Knust⁹, A. LaCluyze¹⁰, B. Milvang-Jensen⁴,
D. Reichart¹⁰, S. Schulze^{17,18}, V. Sudilovsky⁹, S. D. Vergani¹⁹

¹Centre for Astrophysics and Cosmology, Science Institute, University of Iceland, Dunhagi 5, 107 Reykjavík, Iceland

²Department of Particle Physics and Astrophysics, Faculty of Physics, Weizmann Institute of Science, 76100, Rehovot, Israel

³European Southern Observatory, Alonso de Córdova 3107, Casilla 19001, Santiago 19, Chile

⁴Dark Cosmology Centre, Niels Bohr Institute, University of Copenhagen, Juliane Mariés Vej 30, 2100 Copenhagen, Denmark

⁵Instituto de Astrofísica de Andalucía (IAA-CSIC), Glorieta de la Astronomía s/n, 18008 Granada, Spain

⁶Unidad Asociada Grupo Ciencia Planetarias UPV/EHU-IAA/CSIC, Departamento de Física Aplicada I, E.T.S. Ingenieria, Universidad del País Vasco UPV/EHU, Alameda de Urquijo s/n, 48013 Bilbao, Spain

⁷Ikerbasque, Basque Foundation for Science, Alameda de Urquijo 36-5, 48008 Bilbao, Spain

⁸Department of Physics and Astronomy, University of Leicester, University Road, Leicester LE1 7RH, UK

⁹Max-Planck-Institut für extraterrestrische Physik, Giessenbachstraße 1, 85748 Garching, Germany

¹⁰Department of Physics and Astronomy, University of North Carolina at Chapel Hill, Campus Box 3255, Chapel Hill, NC 27599, USA

¹¹Department of Physics, NC A&T State University, 1601 E. Market St, Greensboro, NC 27411

¹²INAF/Rome Astronomical Observatory, via Frascati 33, I-00040 Monteporzio Catone (Roma), Italy

¹³ASI-Science Data Center, Via del Politecnico snc, I-00133 Rome, Italy

¹⁴Zentrum für Astronomie der Universität Heidelberg, Institut für Theoretische Astrophysik, Philosophenweg 12, 69120 Heidelberg, Germany

¹⁵APC, Astroparticule et Cosmologie, Université Paris Diderot, CNRS/IN2P3, CEA/Irfu, Observatoire de Paris, Sorbonne Paris Cité, 10, Rue Alice Domon et Leonie Duquet, F-75205 Paris, Cedex 13, France

¹⁶Anton Pannekoek Institute for Astronomy, University of Amsterdam, Science Park 904, 1098 XH, Amsterdam, The Netherlands

¹⁷Instituto de Astrofísica, Facultad de Física, Pontificia Universidad Católica de Chile, Casilla 306, Santiago 22, Chile

¹⁸Millennium Institute of Astrophysics

¹⁹Laboratoire GEPI, Observatoire de Paris, CNRS-UMR8111, Université Paris Diderot, 5 place Jules Janssen, F-92195 Meudon, France

arXiv:1409.6315v1 [astro-ph.GA] 22 Sep 2014

ABSTRACT

We present the first reported case of the simultaneous metallicity determination of a gamma-ray burst (GRB) host galaxy, from both afterglow absorption lines as well as strong emission-line diagnostics. Using spectroscopic and imaging observations of the afterglow and host of the long-duration GRB 121024A at $z = 2.30$, we give one of the most complete views of a GRB host/environment to date. We observe a strong damped Ly α absorber (DLA) with a hydrogen column density of $\log N(\text{H I}) = 21.80 \pm 0.15$, H₂ absorption in the Lyman-Werner bands (molecular fraction of $\log(f) \approx -1.4$; fourth solid detection of molecular hydrogen in a GRB-DLA), the nebular emission lines H α , H β , [O II], [O III] and [N II], as well as a large variety of metal absorption lines. We find a GRB host galaxy that is highly star-forming (SFR $\sim 40 M_{\odot} \text{ yr}^{-1}$), with a dust-corrected metallicity along the line of sight of $[\text{Zn}/\text{H}]_{\text{corr}} = -0.5 \pm 0.2$ ($[\text{O}/\text{H}] \sim -0.3$ from emission lines), and a depletion factor of refractory elements of $[\text{Zn}/\text{Fe}] = 0.85 \pm 0.04$. The molecular gas is separated by 400 km s^{-1} from the gas that is excited by the GRB (implying a fairly massive host, in agreement with the derived stellar mass of $\log(M_{*}/M_{\odot}) = 9.9^{+0.2}_{-0.3}$). Including emission line analysis, we isolate and characterise three different gas-phases within the star-forming host galaxy. Our main result is that the metallicity determinations from both absorption and emission lines are consistent, which is encouraging for the comparison of GRB host metallicities at different redshifts.

Key words: Galaxies: abundances – gamma-ray burst: individual: GRB 121024A

1 INTRODUCTION

The study of gamma-ray burst (GRB) afterglows has proven to be a powerful tool for detailed studies of the interstellar medium (ISM) of star-forming galaxies, out to high redshifts (e.g. Vreeswijk et al. 2004; Prochaska et al. 2007; Ledoux et al. 2009; Sparre et al. 2014). With quickly fading emission spanning the entire electromagnetic spectrum, GRB afterglows offer a unique opportunity to probe the surrounding environment. The intrinsic spectrum of the afterglow is well fitted with simple power-law segments, so the features of the intergalactic medium (IGM) as well as the ISM surrounding the burst are relatively easy to distinguish from the afterglow in the observed spectrum. With absorption and emission-line analysis it is hence possible to determine parameters such as H I column density, metallicity, dust depletion, star-formation rate (SFR) and kinematics of the GRB host galaxy.

Metallicity is a fundamental parameter for characterising a galaxy and it holds important information about its history. Metallicity might also play a crucial role in the GRB production mechanism. For GRB hosts, the metallicity is measured either from hydrogen and metal absorption lines, or by using diagnostics based on the fluxes of strong nebular

emission lines, calibrated in the local Universe. Different calibrations are in use leading to some discrepancy (e.g., Kudritzki et al. 2012), and the different diagnostics have their strengths and weaknesses (e.g. less sensitive to reddening, multiple solutions, or more sensitive at high metallicities). The absorption lines probe the ISM along the line of sight, while the nebular line diagnostics determine the metallicity of the H II regions of the host. For GRB damped Ly α absorbers (GRB-DLAs), a direct comparison of metallicity from the two methods is interesting as it can either provide a test of the strong-line methods or alternatively allow a measurement of a possible offset in abundances in H II regions and in the ISM. So far, this comparison has only been carried out for galaxy counterparts of DLAs found in the line of sight of background QSOs (QSO-DLAs) (e.g. Bowen et al. 2005; Péroux et al. 2012; Noterdaeme et al. 2012; Fynbo et al. 2013; Jorgenson & Wolfe 2014). A comparison for GRB-DLAs has to our knowledge not been reported before. For this measurement to be feasible with current instrumentation, the observed host needs to be highly star-forming, to have strong nebular lines, and at the same time be at a redshift high enough for the Ly α transition to be observed (at redshifts higher than $z \approx 1.5$ the Ly α absorption line is redshifted into the atmospheric transmission window). GRB 121024A is a $z = 2.30$ burst hosted by a highly star-forming galaxy. We measure abundances of the GRB host galaxy in absorption and compare them with the metallicity determined by strong-line diagnostics using observed nebular lines from [O II], [O III], [N II] and the Balmer emission lines.

Apart from the absorption features from metal lines, we also detect the Lyman-Werner bands of molecular hydrogen. Molecular hydrogen is notoriously hard to detect (in emission) due to the symmetry of the molecule. As long duration GRBs ($t_{\text{obs}} > 2 \text{ s}$) are thought to be associated with the death of massive stars (e.g. Hjorth et al. 2003; Stanek et al.

* Based on observations carried out under prog. ID 090.A-0088(B) with the X-shooter spectrograph installed at the Cassegrain focus of the Very Large Telescope (VLT), Unit 2 – Kueyen, operated by the European Southern Observatory (ESO) on Cerro Paranal, Chile. Also used are observations made with the Nordic Optical Telescope, operated by the Nordic Optical Telescope Scientific Association, and the Gran Telescopio Canarias (program GTC67-13B), both at the Observatorio del Roque de los Muchachos, La Palma, Spain, of the Instituto de Astrofísica de Canarias. HAWK-I imaging used is part of the program 092.A-0076(B). This work made use of data supplied by the UK Swift Science Data Centre at the University of Leicester.

2003; Sparre et al. 2011; Cano 2013; Schulze et al. 2014), they are expected to be found near areas with active star formation, and hence molecular clouds. In spite of this, there are very few detections of molecular absorption towards GRBs. Ledoux et al. (2009) found that this is likely due to the low metallicities found in the systems observed with high resolution spectrographs ($R = \lambda/\Delta\lambda \gtrsim 40000$). As with QSO-DLAs, lines of sight with H_2 will preferentially be metal-rich and dusty. The observed spectra are therefore UV-faint and difficult to observe (GRB 080607 being a striking exception, where observations were possible thanks to its extraordinarily intrinsic luminosity and rapid spectroscopy, see Prochaska et al. 2009). Now with X-shooter (Vernet et al. 2011) on the Very Large Telescope (VLT) we are starting to secure spectra with sufficient resolution to detect H_2 for fainter systems resulting in additional detections (Krühler et al. 2013; D’Elia et al. 2014).

Throughout this paper we adopt a flat Λ CDM cosmology with $H_0 = 71 \text{ km s}^{-1}$ and $\Omega_M = 0.27$, and report 1σ errors (3σ limits), unless otherwise indicated. Reference solar abundances are taken from Asplund et al. (2009), where either photospheric or meteoritic values (or their average) are chosen according to the recommendations of Lodders et al. (2009). Column densities are in cm^{-2} . In Sect. 2 we describe the data and data reduction used in this paper, in Sect. 3 we go through the data analysis and results, which are then discussed in Sect. 4.

2 OBSERVATIONS AND DATA REDUCTION

On 2012 October 24 at 02:56:12 UT the Burst Alert Telescope (BAT, Barthelmy et al. 2005) onboard the *Swift* satellite (Gehrels et al. 2004) triggered on GRB 121024A. The X-Ray Telescope (XRT) started observing the field at 02:57:45 UT, 93 seconds after the BAT trigger. About one minute after the trigger, Skynet observed the field with the PROMPT telescopes located at CTIO in Chile and the 16” Dolomites Astronomical Observatory telescope (DAO) in Italy (Reichart et al. 2005) in filters g', r', i', z' and BRi . Approximately 1.8 hours later, spectroscopic afterglow measurements in the wavelength range of 3000 Å to 25000 Å were acquired (at 04:45 UT), using the cross-dispersed, echelle spectrograph X-shooter (Vernet et al. 2011) mounted at ESO’s VLT. Then at 05:53 UT, 3 hours after the burst, the Gamma-Ray burst Optical/NIR Detector (GROND, Greiner et al. 2007, 2008) mounted on the 2.2 m MPG/ESO telescope at La Silla Observatory (Chile), performed follow-up optical/NIR photometry simultaneously in g', r', i', z' and JHK . About one year later (2013 November 07), VLT/HAWK-I imaging of the host was acquired in the J (07:02:13 UT) and K (06:06:47 UT) band. To supplement these, B , R and i band imaging was obtained at the Nordic Optical Telescope (NOT) at 2014 January 06 (i) and February 10 (R) and 19 (B). Gran Telescopio Canarias (GTC) observations in the g and z band were optioned on 2014 February 28. For an overview see Tables 1 and 2. Linear and circular polarisation measurements for the optical afterglow of GRB 121024A have been reported in Wiersema et al. (2014).

Table 1. X-shooter observations

t_{obs} (UT) ^a	t_{GRB} (min) ^b	$t_{\text{exp.}}$ (s)	Mean Airmass	Seeing
04:47:01	116	600	1.23	0"6-0"7
04:58:35	127	600	1.39	0"6-0"7
05:10:12	139	600	1.31	0"6-0"7
05:21:46	151	600	1.13	0"6-0"7

^a Start time of observation on October 24, 2012.

^b Mid-exposure time in seconds since GRB trigger.

2.1 X-shooter NIR/Optical/UV Spectroscopy

The X-shooter observation consists of four nodded exposures with exposure times of 600 s each, taken simultaneously by the ultraviolet/blue (UVB), visible (VIS) and near-infrared (NIR) arms. The average airmass was 1.18 with a median seeing of 0"7. The spectroscopy was performed with slit-widths of 1"0, 0"9 and 0"9 in the UVB, VIS and NIR arms, respectively. The resolving power $R = \lambda/\Delta\lambda$ is determined from telluric lines to be $R = 13000$ for the VIS arm. This is better than the nominal value due to the very good seeing. Following Fynbo et al. (2011) we then infer $R = 7100$ and $R = 6800$ for the UVB and NIR arms.

X-shooter data were reduced with the ESO/X-shooter pipeline version 2.2.0 (Goldoni et al. 2006), rectifying the data on an output grid with a dispersion of 0.15 Å/pixel in the UVB, 0.13 Å/pixel in the VIS and 0.5 Å/pixel in the NIR arm. The wavelength solution was obtained against arc-lamp frames in each arm. Flux-calibration was performed against the spectrophotometric standard GD71 observed during the same night. For the NIR spectrum we further correct the flux-calibrated spectrum for slit-losses by integrating it over filter curves from GROND photometry in J , H and K bands shifted to X-shooter observation times (assuming a slope of $\alpha = 0.8$). All emission lines are in the NIR spectrum, so only here do we need the absolute flux scale. Wavelengths are plotted in vacuum and corrected for heliocentric motion.

2.2 NOT, GTC and VLT/HAWK-I imaging

To derive physical parameters of the host of GRB 121024A via stellar population synthesis modelling, we obtained late-time photometry from VLT/HAWK-I, NOT and GTC. Exposure times and seeing can be found in Table 2.

J and K band images were observed with HAWK-I on the Yepun (VLT-UT4) telescope at the ESO Paranal Observatory in Chile. HAWK-I is a near-infrared imager with a pixel scale of 0"106/pix and a total field of view of 7'5 × 7'5. B , R and i images were obtained with the ALFOSC optical camera on the NOT. The photometric calibration was carried out by observing the standard star GD71 at a similar airmass to the GRB field. g' and z' -band host galaxy images were taken with the 10.4m GTC. The images were acquired with the OSIRIS instrument which provides an unvignetted field of view of 7'8 × 7'8 and a pixel scale of 0"25/pix (Cepa et al. 2000). Images were taken following a dithering pattern. The z' -band images were defringed by subtracting an interference pattern which was constructed based on the dithered individual frames. The photometric calibration was carried out by observing the standard star

Table 2. Photometric Observations

Instrument	Time ^a	Filter	Exp. time (s)	Seeing	Mag. (Vega)
MPG/GROND	3.0 h	<i>g'</i>	284	1''55	20.79 ± 0.07
MPG/GROND	3.0 h	<i>r'</i>	284	1''40	19.53 ± 0.05
MPG/GROND	3.0 h	<i>i'</i>	284	1''26	19.05 ± 0.07
MPG/GROND	3.0 h	<i>z'</i>	284	1''39	18.66 ± 0.08
MPG/GROND	3.0 h	<i>J</i>	480	1''36	17.84 ± 0.09
MPG/GROND	3.0 h	<i>H</i>	480	1''29	16.98 ± 0.10
MPG/GROND	3.0 h	<i>K_s</i>	480	1''21	16.07 ± 0.11
VLT/HAWK-I	355.2 d	<i>J</i>	240 × 10	0''6	22.4 ± 0.1
VLT/HAWK-I	355.1 d	<i>K</i>	240 × 10	0''5	20.8 ± 0.2
NOT/ALFOSC	483.9 d	<i>B</i>	5 × 480	1''3	24.2 ± 0.2
NOT/ALFOSC	475.0 d	<i>R</i>	9 × 265	1''1	23.8 ± 0.3
NOT/ALFOSC	440.0 d	<i>i</i>	9 × 330	0''9	23.8 ± 0.3
GTC/OSIRIS	491.3 d	<i>g'</i>	3 × 250	1''6	24.9 ± 0.1
GTC/OSIRIS	491.3 d	<i>z'</i>	10 × 75	1''4	23.2 ± 0.3

^a Time since the GRB trigger. For the afterglow measurements time is given in hours, while for the host galaxy, it is shown in days.

SA95-193 (Smith et al. 2002). NOT and GTC are located at the observatory of Roque de los Muchachos, La Palma, Spain.

All images were dark-subtracted and flat-fielded using IRAF standard routines.

2.3 GROND and Skynet Photometry

GROND data was reduced using standard IRAF tasks (Tody 1997; Krühler et al. 2008). The afterglow image was fitted using a general point spread function (PSF) model obtained from bright stars in the field. The optical images in *g'*, *r'*, *i'*, *z'* were calibrated against standard stars in the SDSS catalogue, with an accuracy of ±0.03 mag. The NIR magnitudes were calibrated using stars of the 2MASS catalogue, with an accuracy of ±0.05 mag. Skynet obtained images of the field of GRB 121024A on 2012 October 24-25 with four 16'' telescopes of the PROMPT array at CTIO, Chile, and the 16'' DAO in Italy. Exposures ranging from 5 to 160 s were obtained in the *BVRI* (PROMPT) and *g'r'i'* (DAO) bands, starting at 02:57:07 UT ($t = 55$ s since the GRB trigger) and continuing until $t = 7.3$ h on the first night, and continuing from $t = 20.7 - 25.5$ h on the second night. Bias subtraction and flat-fielding were performed via Skynet's automated pipeline. Post-processing occurred in Skynet's guided analysis pipeline, using both custom and IRAF-derived algorithms. Differential aperture photometry was performed on single and stacked images, with effective exposure times of 5 s to 20 min on the first night, and up to ~4 h on the second night. Photometry was calibrated to the catalogued *BVg'r'i'* magnitudes of five APASS DR7 stars in the field, with *g'r'i'* magnitudes transformed to RI using transformations obtained from prior observations of Landolt stars (Henden, A. et al., in preparation). The Skynet magnitudes can be seen in Appendix A.

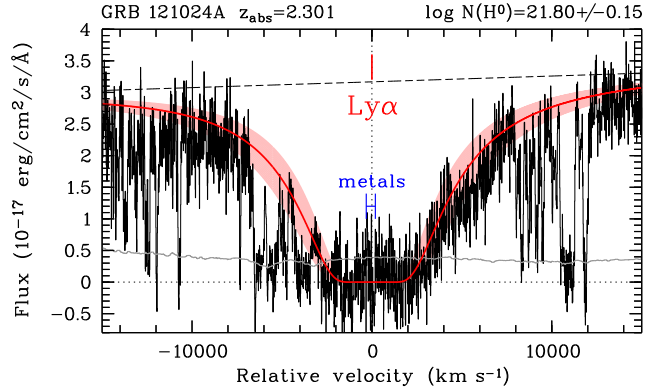


Figure 1. The X-shooter spectra centred on the Ly α absorption lines at the GRB host galaxy redshifts. A neutral hydrogen column density fit ($\log N(\text{HI}) = 21.80 \pm 0.15$) to the damped Ly α line is shown with a solid line (red), while the 1σ errors are shown with the shaded area (also red). In blue is shown the velocity range of the metal absorption lines. The grey line near the bottom shows the error noise.

3 ANALYSIS AND RESULTS

3.1 Absorption Lines

The most prominent absorption feature is the Ly α line. We plot the normalised spectral region in Fig. 1. Over-plotted is a Voigt-profile fit to the strong Ly α absorption line yielding $\log N(\text{HI}) = 21.80 \pm 0.15$. To determine the ionic column densities of the metals, we modelled the identified absorption lines with a number of Voigt-profile components, as follows. We use the Voigt-profile fitting software VPFIT¹ version 9.5 to model the absorption lines. We first normalise the spectrum around each line, fitting featureless regions with zero- or first-order polynomials. To remove the contribution of atmospheric absorption lines from our Voigt-profile fit, we compare the observed spectra to a synthetic

¹ <http://www.ast.cam.ac.uk/~rfc/vpfit.html>

Table 3. Ionic column densities of the individual components of the line profile. The transitions used to derive column densities are reported in the second column. Transitions marked in bold are those unblended and unsaturated lines that we use to determine the line-profile decomposition. The results for the ground state and excited levels are listed in the top and bottom part of the table, respectively. Velocities given are with respect to the [O III] $\lambda 5007$ line. (b) / (s) indicate that the line is blended / saturated.

Component	Transition	a	b	c	d	e
z	—	2.2981	2.2989	2.3017	2.3023	2.3026
b (km s $^{-1}$)	—	26	21	20	22	35
v (km s $^{-1}$)	—	-264	-191	63.6	118	145
$\log(N/\text{cm}^{-2})$						
Mg I	$\lambda 1827, \lambda 2026(\text{b})$	13.97 ± 0.04	13.57 ± 0.04	< 13.4	13.57 ± 0.07	< 13.4
Al III	$\lambda 1854(\text{s}), \lambda 1862(\text{s})$	—	—	—	—	—
Si II	$\lambda 1808$	—	—	—	—	—
S II	$\lambda 1253(\text{s})$	—	—	—	—	—
Ca II	$\lambda 3934, \lambda 3969$	13.25 ± 0.16^a	12.50 ± 0.16^b	12.20 ± 0.16	11.90 ± 0.16	11.20 ± 0.16
Cr II	$\lambda 2056, \lambda 2062(\text{b}), \lambda 2066$	13.47 ± 0.03	13.48 ± 0.03	13.39 ± 0.03	13.67 ± 0.04	13.34 ± 0.09
Mn II	$\lambda 2576, \lambda 2594, \lambda 2606$	13.15 ± 0.01	13.07 ± 0.01	12.71 ± 0.03	13.21 ± 0.02	12.93 ± 0.04
Fe II	$\lambda 1611, \lambda 2260, \lambda 2249$	15.15 ± 0.02	15.09 ± 0.02	14.81 ± 0.04	15.27 ± 0.03	15.12 ± 0.05
Ni II	$\lambda 1345, \lambda 1454, \lambda 1467.3, \lambda 1467.8, \lambda 1709$	13.91 ± 0.10	13.88 ± 0.10	13.95 ± 0.09	14.17 ± 0.10	13.73 ± 0.29
Zn II	$\lambda 2026(\text{b}), \lambda 2062(\text{b})$	13.14 ± 0.03	13.05 ± 0.03	12.50 ± 0.08	13.40 ± 0.03	12.19 ± 0.40
Component		α	β			
z	—	2.2981	2.2989	—	—	—
b (km s $^{-1}$)	—	28	30	—	—	—
v (km s $^{-1}$)	—	-264	-191	—	—	—
Fe II 1s	$\lambda 2389, \lambda 2396(\text{b})$	13.25 ± 0.02	13.16 ± 0.03	—	—	—
Fe II 2s	$\lambda 2396(\text{b}), \lambda 2405(\text{b}), \lambda 2607$	12.92 ± 0.04	12.80 ± 0.04	—	—	—
Fe II 3s	$\lambda 2405(\text{b}), \lambda 2407, \lambda 2411(\text{b})$	12.63 ± 0.05	12.58 ± 0.07	—	—	—
Fe II 4s	$\lambda 2411(\text{b}), \lambda 2414, \lambda 2622$	12.53 ± 0.06	12.61 ± 0.05	—	—	—
Fe II 5s	$\lambda 1559, \lambda 2360$	13.95 ± 0.08	13.68 ± 0.13	—	—	—
Ni II**	$\lambda 2166, \lambda 2217, \lambda 2223$	13.43 ± 0.02	13.47 ± 0.02	—	—	—
Si II*	$\lambda 1309, \lambda 1533, \lambda 1816^e$	14.98 ± 0.11^c	14.39 ± 0.04^d	—	—	—

^a redshift: 2.2979, b -value: 30 km s $^{-1}$

^b redshift: 2.2989, b -value: 23 km s $^{-1}$

^c redshift: 2.2979, b -value: 20 km s $^{-1}$

^d redshift: 2.2987, b -value: 30 km s $^{-1}$

^e The column density of the α component of Si II* has been determined solely from the $\lambda 1816$ line.

Table 4. Total column densities (summed among individual velocity components and including excited levels) and abundances with respect to H and Fe.

Ion	$\log(N/\text{cm}^{-2})_{\text{tot}}$	$\log(N/\text{cm}^{-2})_{\text{a+b}}$	$\log(N/\text{cm}^{-2})_{\text{c+d+e}}$	$[\text{X}/\text{H}]_{\text{tot}}$	$[\text{X}/\text{Fe}]$	$[\text{X}/\text{Fe}]_{\text{a+b}}$	$[\text{X}/\text{Fe}]_{\text{c+d+e}}$
H I	21.80 ± 0.15	—	—	—	—	—	—
Mg I	< 14.31	14.11 ± 0.03	< 13.86	—	—	—	—
Al III	> 14.11	—	—	> -2.1	> -0.66	—	—
Si II	> 16.35	—	—	> -1.0	> 0.53	—	—
S II	> 15.90	—	—	> -1.0	> 0.46	—	—
Ca II	13.37 ± 0.12	13.32 ± 0.13^a	12.40 ± 0.12	-2.8 ± 0.2	-1.29 ± 0.12	-0.97 ± 0.14^a	-2.02 ± 0.11
Cr II	14.18 ± 0.02	13.78 ± 0.02	13.97 ± 0.02	-1.3 ± 0.2	0.22 ± 0.04	0.18 ± 0.03	0.24 ± 0.03
Mn II	13.74 ± 0.01	13.41 ± 0.01	13.47 ± 0.01	-1.5 ± 0.2	-0.01 ± 0.03	0.03 ± 0.02	-0.04 ± 0.02
Fe II	15.82 ± 0.03	15.45 ± 0.02	15.58 ± 0.02	-1.5 ± 0.2	—	—	—
Ni II	14.70 ± 0.06	14.33 ± 0.05	14.47 ± 0.06	-1.3 ± 0.2	0.17 ± 0.06	0.02 ± 0.05	0.16 ± 0.06
Zn II	13.74 ± 0.02	13.40 ± 0.03	13.47 ± 0.04	-0.6 ± 0.2	0.85 ± 0.04	0.88 ± 0.03	0.83 ± 0.03

^a Different a and b broadening parameter and redshift for Ca II, see Sect. 3.1

telluric spectrum. This telluric spectrum was created following Smette et al. (2010) as described by De Cia et al. (2012) and assuming a precipitable water-vapour column of 2.5 mm. We systematically reject from the fit the spectral regions affected by telluric features at a level of > 1 per cent². None of the absorption lines that we include are severely affected by telluric lines. The resulting column densities are listed in Tables 3 and 4 for lines arising from ground-state and excited levels. The Voigt-profile fits to the metal lines are shown in Figs. 2 and 3.

The fit of the ground-state lines is composed of five components (a-e). Compared to the redshift of the emission line [O III] $\lambda 5007$, components 'a' through 'e' are shifted -264 , -191 , 63.6 , 118 and 145 km s^{-1} , respectively. Given the resolution of the instrument of 23 km s^{-1} (VIS arm), the individual components are blended, and therefore the profile decomposition is not unequivocal. However, regardless of the properties (and numbers) of the individual components, they are clearly divided into two well separated groups: a+b and c+d+e (when forcing more components to the fit of each group, the resultant total column density stayed the same for each of the two groups. We stress that the resultant b-values are not physical, but likely a combination of smaller unresolved components). To determine fit-parameters redshift, z and broadening parameter, b (purely turbulent broadening) of the individual components of the line profile, a preliminary fit was made with a master-sample of unblended and unsaturated lines (shown in bold in Table 3), with b and z linked between the lines. Values for z and b were then frozen for the rest of the absorption lines, and the column densities were fitted. $3\text{-}\sigma$ lower and upper limits are given for the saturated and undetected components, respectively. For the saturated lines Al III, Si II and S II we do not report column densities from the Voigt-profile fit, but instead from the measured equivalent widths (EWs), converted to column densities assuming a linear regime. For these, we only report the total column density for all the components together, as the individual EW of each component is difficult to measure.

At the H I column density observed, we expect most elements to be predominantly in their singly ionised state (Wolfe et al. 2005). We hence expect much of the Mg to be in Mg II (for this reason we do not report metallicity and depletion factor for Mg I in Table 4). Ca II seems to have a different velocity composition than the rest of the lines. One possibility is that Ca II may extend to a slightly different gas phase, as its ionisation potential is the lowest among the observed lines (less than 1 Ryd). Alternatively, since the Ca II lines are located in the NIR arm, a small shift in the wavelength solution with respect to the VIS arm could cause the observed difference. Based on the comparison of skylines, however, no such shift is evident in our data. We have allowed z and b to have different values for the two Ca II lines. This resulted in a slightly different a+b component, but the same c+d+e component as for the rest of the sample.

The fine-structure lines show a different velocity profile composed only of two components, α and β , see Table 3. The redshift of α and β are the same as for component a

and b found for the resonance lines (but different broadening parameters). Remarkably, no fine-structure lines are detected at the position of components c+d+e. Si II* lines are poorly fitted when tied together with the rest of the fine-structure lines, so we allowed their z and b values to vary freely. We note that Si II* $\lambda 1309$ and $\lambda 1533$ are observed in the UVB arm, while the other fine structure lines (except Fe II 5s $\lambda 1559$) are from the VIS arm. Hence, it is again possible that the slight shift in wavelength between the two arms are the cause of the difference in velocity. The column density for component α of the stronger Si II* line appears strongly saturated, so only the $\lambda 1816$ line has been used to determine the column density in this component.

The total ionic column densities (summed over individual components and including excited levels when necessary) are given in Table 4. We also report the column densities of the groups of component a+b and c+d+e, which are well resolved from each other, unlike the individual components. Our best constraint on the metallicity is from Zn, as this element is usually not depleted (or has a low depletion) into dust (see e.g. Pettini et al. 1994). We derive $[\text{Zn}/\text{H}] = -0.6 \pm 0.2$ (the other low-depletion elements Si and S are saturated, but the limits we found are consistent). This agrees well with the gas-phase metallicity found from the emission line fluxes (see Sect. 4.1).

We note that high ionisation lines from N V, Si IV as well as C IV are detected, but are highly saturated.

3.2 Dust Depletion

Refractory elements, such as Fe, Ni, and Cr, are typically heavily depleted into dust grains (e.g., Savage & Sembach 1996; Ledoux et al. 2002b), and the gas-phase abundances that we measure from the absorption lines are thus lower than from for instance Zn. A first indicator of the level of depletion in the ISM is the relative abundance $[\text{Zn}/\text{Fe}]$ (referred to as the depletion factor), because Zn is marginally if not at all depleted into dust grains. We measure $[\text{Zn}/\text{Fe}] = 0.85 \pm 0.04$, which indicates a fairly high amount of dust. This value is quite typical for GRB- and QSO-DLAs at the metallicity $[\text{Zn}/\text{H}] = -0.6 \pm 0.2$ that we measure (e.g., see the abundances in Noterdaeme et al. 2008). Following De Cia et al. (2013) we calculate a column density of Fe in dust-phase of $\log N(\text{Fe})_{\text{dust}} = 16.74 \pm 0.14$ and a dust-corrected metallicity of $[\text{Zn}/\text{H}]_{\text{corr}} = -0.5 \pm 0.2$, indicating that even Zn is mildly depleted in this absorber, by ~ 0.1 dex. This is not surprising given the level of depletion, as also discussed by Jenkins (2009).

We also compare the observed abundances of a variety of metals (namely Zn, S, Si, Mn, Cr, Fe, and Ni) to the depletion patterns of a warm halo (H), warm disk+halo (DH), warm disk (WD) and cool disk (CD) types of environments, as defined in Savage & Sembach (1996). These are fixed depletion patterns observed in the Galaxy and calculated assuming that Zn is not depleted into dust grains. We fit the observed abundances to the depletion patterns using the method described in Savaglio (2001). We find that none of the environments are completely suitable to describe the observed abundances. The fits to a cool- and warm-disk patterns are displayed in Fig. 4 ($\chi^2_{\nu} = 0.64$ and 0.86 , respectively, while $\chi^2_{\nu} = 1.45$ and 1.55 for a disk+halo and a halo pattern). For the cool disk the lower limit on the Si column

² This procedure does not aim at reproducing the observed telluric spectrum, but simply reject suspect telluric lines from the Voigt-profile fit.

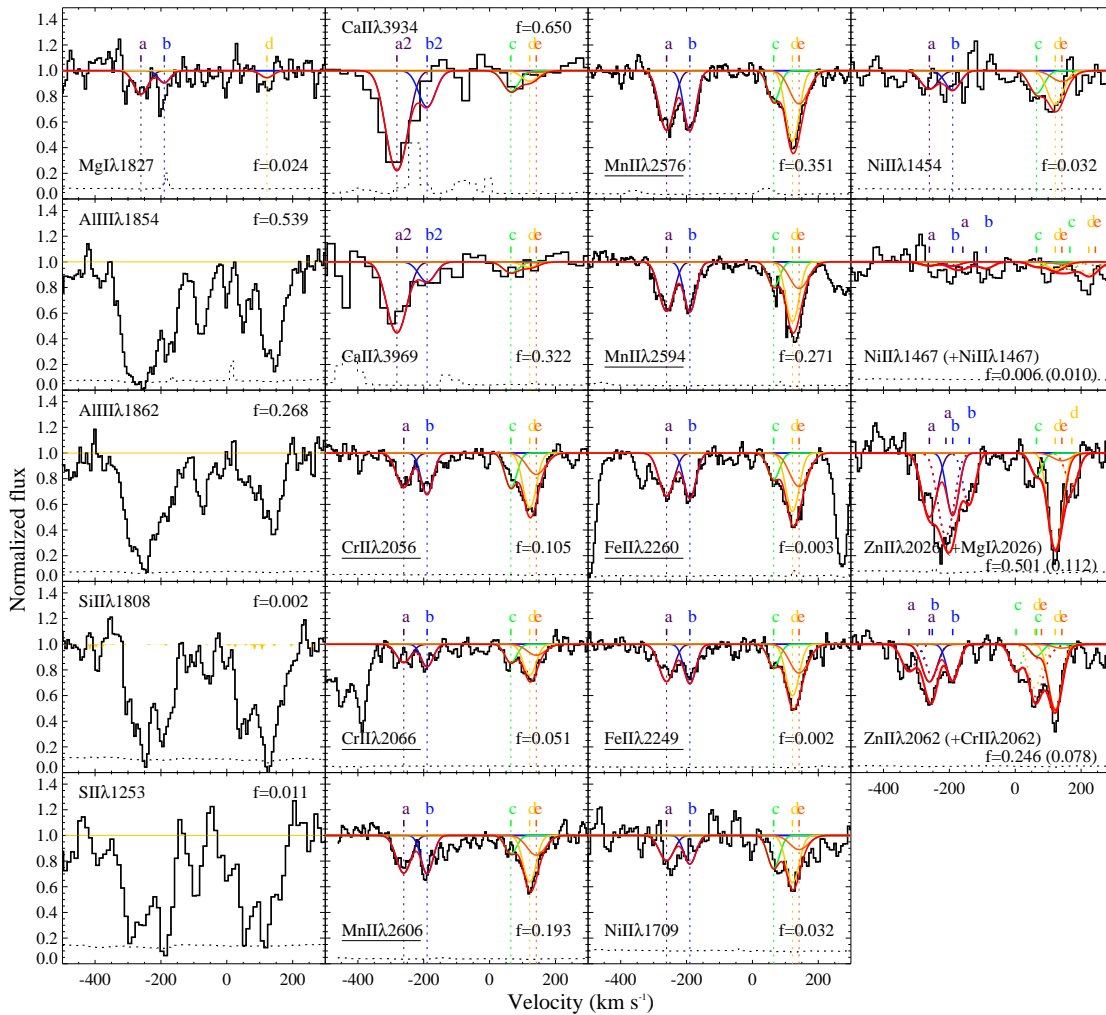


Figure 2. Velocity profiles of the metal resonance lines. Black lines show the normalised spectrum, with the associated error indicated by the dashed line at the bottom. The Voigt-profile fit to the lines is marked by the red line, while the single components of the fit are displayed in several colours (vertical dotted lines mark the centre of each component). The decomposition of the line-profile was derived by modelling only the underlined transitions. The oscillator strength is labelled in each panel. Saturated lines have not been fitted with a Voigt-profile, so for these we show only the spectrum. See online version for colours.

density is not very well reproduced, while the fit for the warm disk overshoots the Mn abundance. The real scenario could be somewhere in between these two environment, or alternatively there are some nucleosynthesis effects which we cannot constrain for our case.

Another quantity that is very useful to derive from the observed dust depletion is the dust-to-metals ratio (DTM , normalised by the Galactic value). Constraining the DTM distribution on a variety of environments can indeed shed light on the origin of dust (e.g. Mattsson et al. 2014). Based on the observed $[Zn/Fe]$ and following De Cia et al. (2013), we calculate $DTM = 1.01 \pm 0.03$, i.e. consistent with the Galaxy. From the depletion-pattern fit described above we derive similar, although somewhat smaller, $DTM = 0.84 \pm 0.03$ (CD) and $DTM = 0.89 \pm 0.03$ (WD). These values are in line with the distribution of the DTM with metallicity and metal column densities reported by De Cia et al. (2013), and are also consistent with the results of Zafar & Watson (2013). Following Zafar & Watson

(2013), we calculate $DTM = 0.1$ based on the dust extinction A_V modelled from the SED fit (Sect. 3.9). Due to the small amount of reddening in the SED, this DTM value is a factor of 10 lower than expected at the metal column densities observed. This will be discussed further in Sect. 4.4.

At the metallicity of GRB 121024A ($\sim 1/3$ solar), it is not possible to draw further conclusions on the dust origin based on the DTM . Both models of pure stellar dust production and those including dust destruction and grain growth in the ISM converge to high (Galactic-like) DTM values at metallicities approaching solar (Mattsson et al. 2014).

3.3 Distance between GRB and Absorbing Gas

The most likely origin of the fine-structure transitions observed in the a+b ($\alpha+\beta$) component, is photo-excitation by UV photons from the GRB afterglow itself (see e.g. Prochaska et al. 2006; Vreeswijk et al. 2007). Assuming the afterglow to be the only source of excitation, we model the

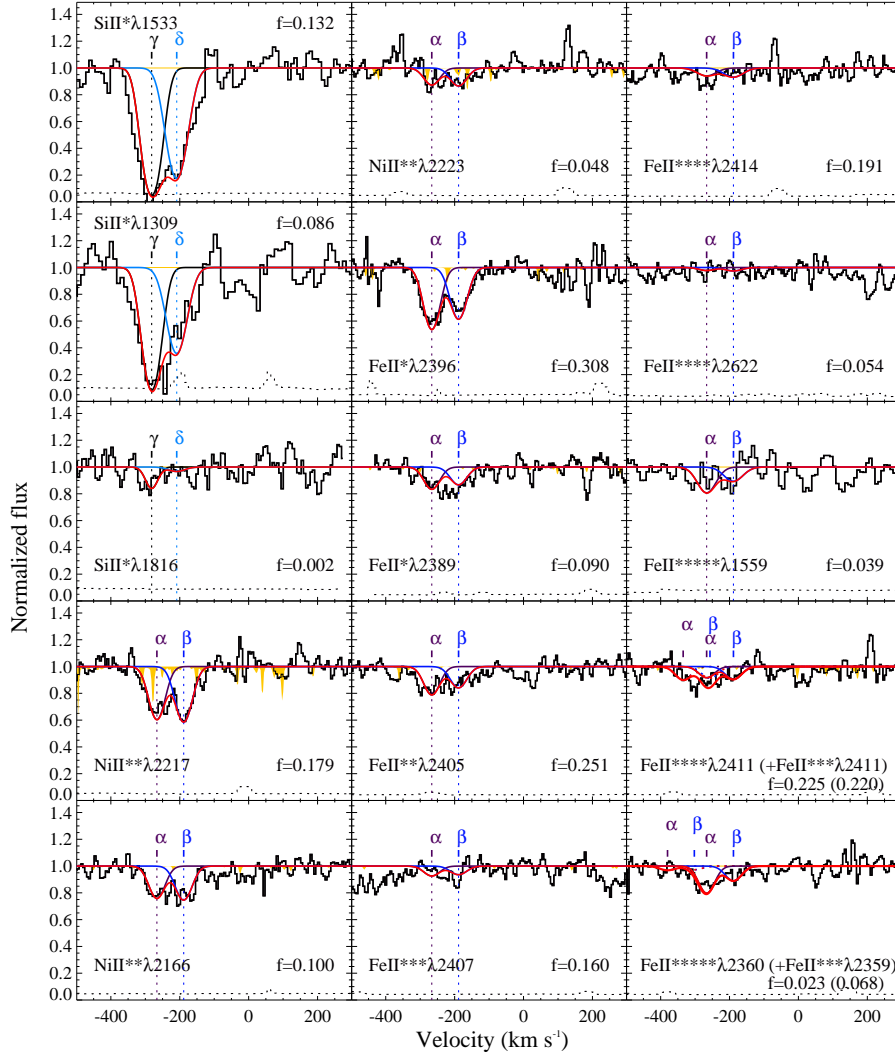


Figure 3. The same as Fig. 2, but for fine-structure lines. Telluric features are highlighted in yellow.

population of the different levels of Fe and Ni, closely following Vreeswijk et al. (2013). Using an optical light curve to estimate the luminosity of the afterglow, we can then determine how far the excited gas must be located from the GRB site, for the afterglow to be able to excite these levels. We model the total column density from component a+b ($\alpha+\beta$) of the Ni II, Ni II** and the five lowest levels of Fe II. We input the optical light curve from Skynet, see Fig. 5 and Tables in Appendix A, which is extrapolated to earlier times using the power-law decay observed. The broadening parameters b from the Voigt-profile fits are used, and we ensured that the atomic data used in these fits (see Sect. 3.1) is consistent with the atomic data used in the modelling (see Vreeswijk et al. 2013).

The best fit (see Fig. 6) is obtained with a distance of 700 ± 60 pc between the cloud and burst, and a cloud size of < 450 pc (2σ). The resultant fit is rather poor ($\chi^2/\text{d.o.f.} = 21.6/3$). As can be seen in Fig. 2 and 3, the column densities of the ground level of Ni II (as probed by Ni II $\lambda\lambda$ 1709, 1454, 1467) and 5th excited level of Fe II (as probed by Fe II 5s $\lambda\lambda$ 1559, 2360) are not very well con-

strained due to the observed spectrum having a low S/N ratio near those features. The formal errors from the Voigt profile fit are likely an underestimate of the true error for these column densities. This, in turn, results in the χ^2 of the excitation model fit being overestimated. Furthermore the lack of spectral time series means the resultant parameters are not well constrained. For the c+d+e component we are able to set a lower limit of 1.9 kpc on the distance to the burst using Fe II, and 3.5 kpc using Si II. Since Si II is saturated, we use the EW to determine the column density, but that only gives the total value of all components together. Hence, for the c+d+e component we fitted using VPFIT and compared the total column density with what we get from the EWs. After establishing that both fits yield the same result, we feel confident in using the column density of $\log N(\text{Si II})_{\text{c+d+e}} > 15.99$ together with a detection limit $\log N(\text{Si II}^*)_{\text{c+d+e}} < 12.18$ on the 1265 Å line, as this is the strongest of the Si II* lines.

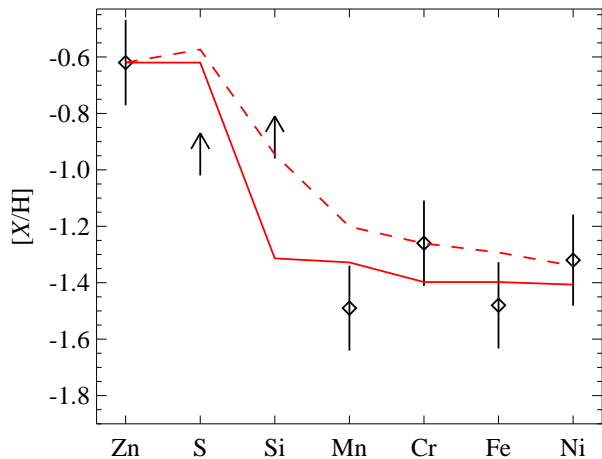


Figure 4. The dust-depletion pattern fit for a cold disk (red solid curve) and a warm disk (red dashed curve) to the observed abundances measured from absorption-line spectroscopy (diamonds and arrows, for the constrained and 3σ limits, respectively).

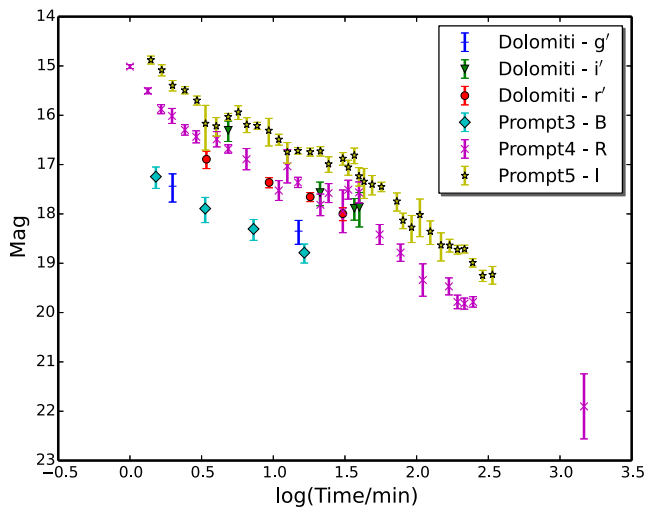


Figure 5. Light curve from the Skynet instruments, used as input for the population modelling. The legend gives the instrument and observational band. Observations started 55s after the GRB trigger. See online version for colours.

3.4 Molecular Hydrogen

We detect Lyman-Werner absorption bands of molecular hydrogen at redshift $z = 2.3021$ (d-component only) in rotational levels $J=0, 1, 2$ and 3 , see Fig. 7. The fitting and analysis of the molecular hydrogen transitions follows Ledoux et al. (2002b, 2003) and Krühler et al. (2013). We performed a Voigt-profile fit of lines mainly from the Lyman bands $L=0-0$ up to $0-3$, as these are found in the less noisy part of the spectrum (a few $J=2$ and 3 lines from the Lyman bands $L=0-4$ and $0-5$ were also fitted). $J=0$ and 1 lines are strong and fairly well constrained by the presence of residual flux around them hinting at damping wings in $L \geq 1$. Given the low spectral resolution of the data and the possibility of hidden saturation, we tested a range of

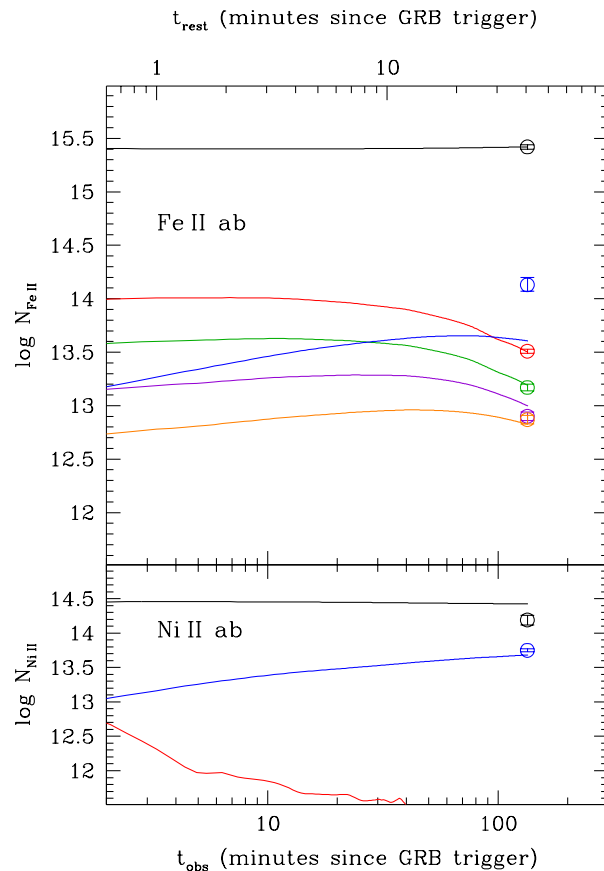


Figure 6. Best-fit model for the excited-level populations of the $a+b$ ($\alpha+\beta$) column densities of Fe II (top panel) and Ni II (bottom). Black lines show the fit to the resonance level. For Fe II, from the lower levels and up, excited-level population are shown with red, green, purple, orange and blue. For Ni II the red line shows the first excited level, while the blue line shows the second. Open circles show the actual values from Voigt-profile fits. See online version for colours.

Doppler parameters. The approximate H_2 column densities, $\log(N(H_2)/\text{cm}^{-2})$ are given in Table 5 for Doppler parameter values of $b = 1$ and 10 . Using the column density of neutral hydrogen for component 'c+d+e' of $\log N(HI) = 21.5$, calculated assuming the same Zn metallicity for the two main velocity components ('a+b' and 'c+d+e'), this results in a molecular fraction in the order of $\log f \sim -1.4$, where $f = 2N(H_2)/(N(HI)+2N(H_2))$. For a redshift of $z \sim 2.2987$ (comp. 'a+b') we find a conservative upper limit on detection of $\log N(H_2) \sim 18.9$. A more detailed analysis is not possible because of the high noise-level. The implications of this detection is discussed in Sect. 4.2.

We searched for vibrationally-excited H_2 by cross-correlating the observed spectrum with a theoretical model from Draine (2000) and Draine & Hao (2002) similar to the procedure outlined in Krühler et al. (2013). There is no evidence for H_2^* in our data, neither through the cross-correlation nor for individual strong transitions, and we set an upper limit of 0.07 times the optical depth of the input model. This approximately corresponds to $\log NH_2^* < 15.7$. A column density of H_2^* as high as seen in e.g.,

Table 5. Estimated column densities for H₂ for broadening parameter values $b = 10$ and $b = 1$ (km s⁻¹).

Rotational level	log($N(\text{H}_2)/\text{cm}^{-2}$)	
	$b = 10 \text{ km s}^{-1}$	$b = 1 \text{ km s}^{-1}$
$J = 0$	19.7	19.7
$J = 1$	19.2	19.3
$J = 2$	16.1	18.3
$J = 3$	16.0	18.2
Total	19.8	19.9

GRBs 120815A or 080607 (Sheffer et al. 2009) would have been clearly detected in our data.

We furthermore note that CO is not detected. We set a conservative limit of $\log N(\text{CO}) < 14.4$, derived by using four out of the six strongest CO AX bandheads with the lowest 6 rotational levels of CO. The wavelength range of the other two bandheads are strongly affected by metal lines, and thus do not provide constraining information.

3.5 Emission Lines

In the NIR spectrum, we detect H α , H β , the [O II] $\lambda\lambda 3727, 3729$ doublet, [N II] $\lambda 6583$ (highest-redshift [N II] detection published for a GRB host) and the two [O III] $\lambda\lambda 4959, 5007$. Table 6 shows the fluxes (extinction-corrected, see Sect. 3.8). The fluxes reported are Gaussian fits, with the background tied between the [O III] doublet and H β , and for H α with [N II], assuming a slope of 0.8. [O II] is intrinsically a doublet, so we fit a double Gaussian with a fixed wavelength spacing based on the wavelength of the rest-frame lines. Using the GROND photometry, we estimate a slit-loss correction factor of 1.25 ± 0.10 . Fig. 8 shows the emission line profiles, the 2D as well as the extracted 1D spectrum. The figure show a Gaussian fit to the lines, after subtracting the PSF for the continuum (done by fitting the spectral trace and PSF as a function of wavelength locally around each line, see Møller (2000) for details). For the weaker [N II], a formal χ^2 minimalisation is done by varying the scale of a Gaussian with fixed position and width. The noise is estimated above and below the position of the trace (marked by a horizontal dotted line in Fig. 8). We assign the zero-velocity reference at the redshift of the [O III] $\lambda 5007$ line. For the weaker [N II] line, we fix the Gaussian-profile fit to be centred at this zero-velocity.

3.6 Star-Formation Rate

The SFR can be derived from the emission line fluxes of H α and [O II]. Using conversion factors from Kennicutt (1998), but converted from a Salpeter initial mass function (IMF) to Chabrier (Treyer et al. 2007), we report extinction corrected (see Sect. 3.8) values of $\text{SFR} = 42 \pm 11 M_{\odot} \text{ yr}^{-1}$ from the H α flux and a $\text{SFR} = 53 \pm 15 M_{\odot} \text{ yr}^{-1}$ derived from [O II]. For a comparison with results from the stellar population synthesis modelling see Sect. 3.10.

Table 6. Measured emission-line fluxes

Transition	Wavelength ^a	Flux ^b	Width ^c	Redshift
[O II]	3726.03, 3728.82	14.5 ± 1.2	— ^d	2.3015 ^e
H β	4861.33	7.4 ± 0.4	218 ± 12	2.3012
[O III]	4958.92	9.0 ± 0.4	194 ± 28	2.3017
[O III]	5006.84	27.2 ± 0.7	192 ± 7	2.3010
H α	6562.80	21.0 ± 1.5	279 ± 17	2.3010
[N II]	6583.41	1.9 ± 0.7	~ 140	— ^f

^a Wavelengths in air in units of Å.

^b Extinction corrected flux in units of $10^{-17} \text{ erg s}^{-1} \text{ cm}^{-2}$.

^c FWHM of line (after removing instrumental broadening) in units of km s⁻¹. Errors do not include uncertainty in continuum.

^d [O II] is intrinsically a doublet, which is not fully resolved here, so we do not give the width.

^e Calculated using a weighted wavelength average of 3727.7 \AA .

^f The Gaussian fit shown of [N II] has a redshift frozen to that of the [O III] $\lambda 5007$ line.

3.7 Metallicity from Emission Lines

We determine the gas-phase metallicity of the GRB host galaxy using the strong-line diagnostics R₂₃, O3N2 and N2 (for a discussion of the different diagnostics see e.g. Kewley & Ellison 2008, note that different metallicity calibrators give different values of metallicity, R₂₃ appears to be consistently higher than O3N2 and N2). The R₂₃ diagnostic has two branches of solutions, but the degeneracy can be broken using the ratios [N II]/H α or [N II]/[O II]. In our case [N II]/H α = 0.09 ± 0.02 and [N II]/[O II] = 0.13 ± 0.03 , which places the solution on the upper branch (though not far from the separation). Because of the large difference in wavelength of the emission lines used for R₂₃, this method is sensitive to the uncertainty of the reddening. Both O3N2 and N2 use lines that are close in wavelength, so for these, we expect the reddening to have a negligible effect. Instead, they then both depend on the weaker [N II] line, which has not got as secure a detection. However all three methods agree within errors: $12 + \log(\text{O}/\text{H}) = 8.6 \pm 0.2$ for R₂₃ (McGaugh 1991), $12 + \log(\text{O}/\text{H}) = 8.2 \pm 0.2$ for O3N2 and $12 + \log(\text{O}/\text{H}) = 8.3 \pm 0.2$ for N2 (both from Pettini & Pagel 2004, the scatter in N2 is likely underestimated). The errors include the scatter in the relation (these values are from Kewley & Ellison 2008, and references therein). See Sect. 4.1 for a comparison with absorption-line metallicity.

3.8 Balmer Decrement

The ratio of the Balmer lines H α and H β can be used to estimate the dust extinction. We use the intrinsic ratio found in the literature (Osterbrock 1989), $I(\text{H}\alpha)/I(\text{H}\beta) = 2.86$, for star-forming regions, where we expect GRBs to occur. The ratio we measure is 2.98 which, assuming the extinction law of Calzetti et al. (2000), results in $E(B - V) = 0.04 \pm 0.09$. We note that adopting a different extinction law (from e.g. Pei 1992) results in the same reddening correction within errors, as there is little difference within the wavelength range of the Balmer lines. We use the Calzetti et al. (2000) law, which is an attenuation law for star burst galaxies, where the Pei (1992) laws are relevant for lines of sight for point-

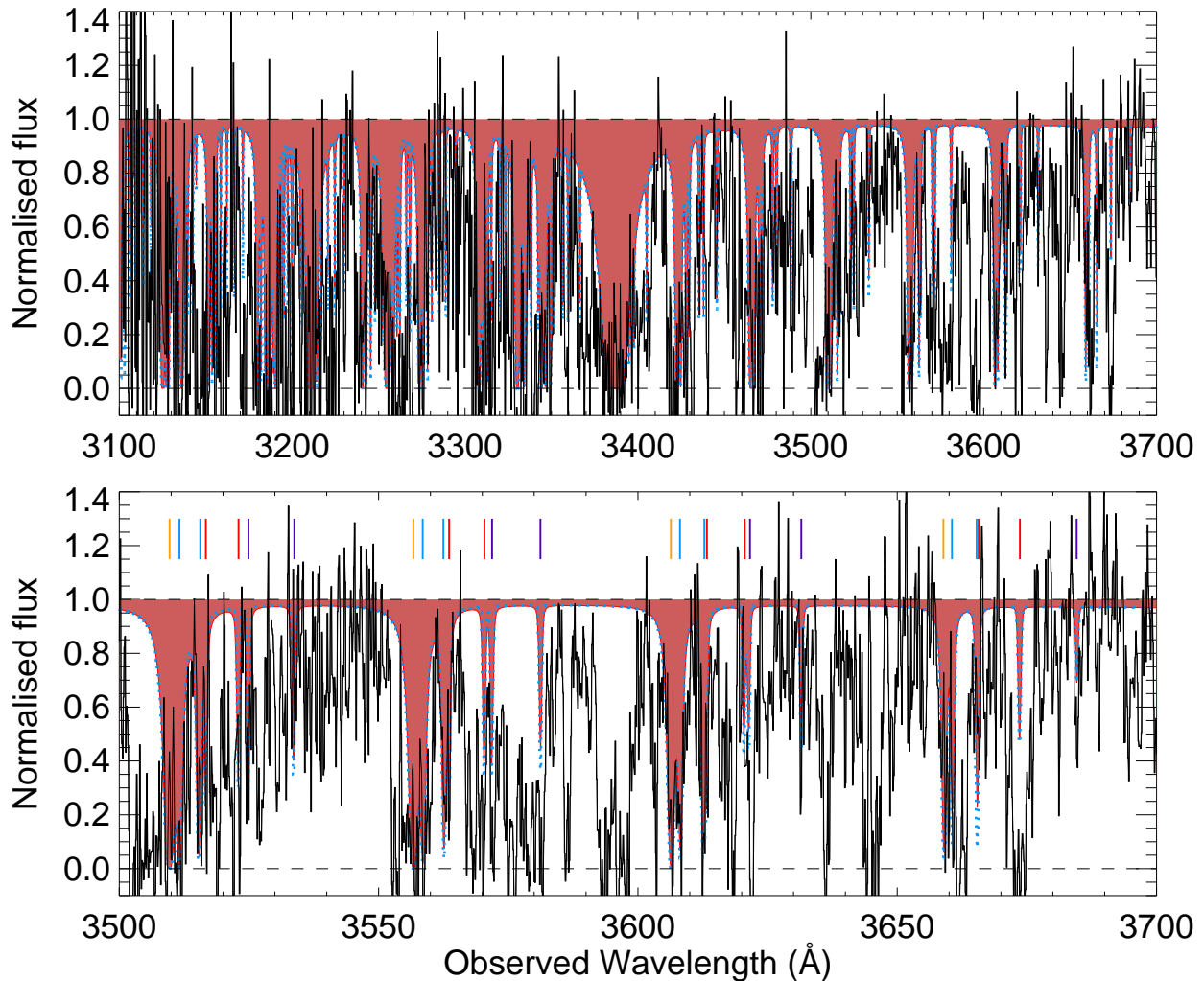


Figure 7. X-shooter spectrum showing Lyman-Werner absorption bands. Top panel shows the full fitted spectrum on the blue side of the $\text{Ly}\alpha$ transition. Bottom panel is a zoomed in region of the spectrum. Top spectrum has been smoothed and re-binned for illustrative purposes. The shaded area shows the synthetic spectrum from a fit with Doppler parameter $b = 1 \text{ km s}^{-1}$, while the blue-dotted line shows the fit for $b = 10 \text{ km s}^{-1}$. In the bottom panel coloured lines show the different transitions. $J=0,1,2$ and 3 is coloured in yellow, blue, red and purple, respectively. See online version for colours.

sources inside galaxies where light is lost due to both absorption and scattering out of the line of sight.

3.9 Broad-Band Spectral Energy Distribution

We fitted the broad-band afterglow data from XRT and GROND (without the g' -band, due to possible DLA contamination), where simultaneous data exist (11 ks after the trigger). The fit was performed within ISIS (Houck & Denicola 2000) following the method of Starling et al. (2007). The XRT data were extracted using *Swift* tools. Single and broken power-law (cooling break) models were used, with two absorbers, one Galactic held fixed at $N(\text{H})_{\text{X}}^{\text{Gal}} = 7.77 \times 10^{20} \text{ cm}^{-2}$ (Willingale et al. 2013), and one intrinsic to the

host galaxy³. The abundances used are from Wilms et al. (2000). An SMC dust-extinction model was used for the host, while the reddening from the Galaxy was fixed to $E(B - V) = 0.123$ (Schlegel et al. 1998). Statistically a single power-law is preferred ($\chi^2 / \text{d.o.f} = 1.07$), see Fig. 9, but with respect to the absorption, the two models give similar results.

Best fit parameters for the single power-law SMC absorption model are $N(\text{H})_{\text{X}} = (1.2_{-0.6}^{+0.8}) \times 10^{22} \text{ cm}^{-2}$ and $E(B - V) = 0.03 \pm 0.02$ at a redshift of $z = 2.298$, and a power-law index of $\beta = 0.90 \pm 0.02$ (90 per cent confi-

³ We assume solar metallicity, not to provide a physical description of the absorbers, but purely to let $N(\text{H})_{\text{X}}$ conform to the standard solar reference.

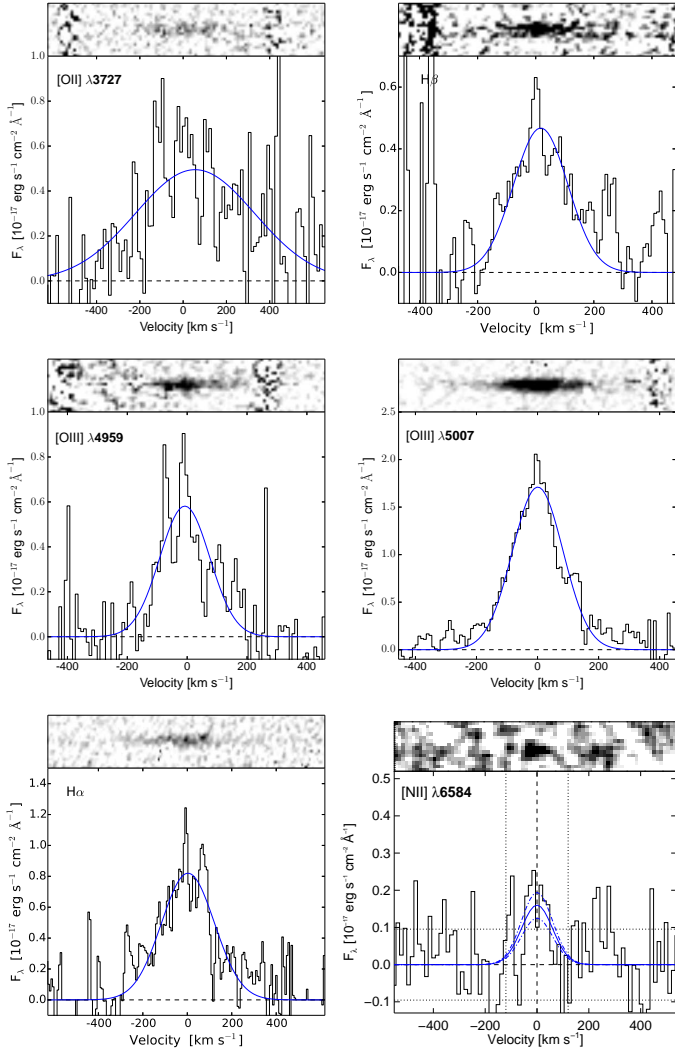


Figure 8. Emission lines detected from the GRB 121024A host. Each panel shows the 2D spectrum after continuum PSF subtraction on top. The bottom part shows the extracted 1D spectrum. The blue line shows the Gaussian fit to the line profile. The abscissa shows the velocity dispersion with respect to the [O III] $\lambda 5007$ reference frame. The [N II] spectrum has been smoothed and binned differently than the other lines, and the fit has been performed with the Gaussian profile centre frozen at 0 km s^{-1} with respect to the reference frame, as indicated with the dashed line in the figure. [O II] has been fit as a doublet for the flux estimate.

dence limits). LMC and MW model fits result in the same values within errors. These values are considered to be upper limits to the host’s optical extinction, due to the presence of foreground absorbers, see Sect. 3.12, which may contribute to the extinction. For a discussion on the extinction see Sect. 4.4.

3.10 Stellar Population Synthesis Modelling

Using our deep photometry of the host, we perform stellar population synthesis modelling of the host galaxy. We use a grid of stellar evolution models with different star formation timescales, age of stellar population and extinction, to com-

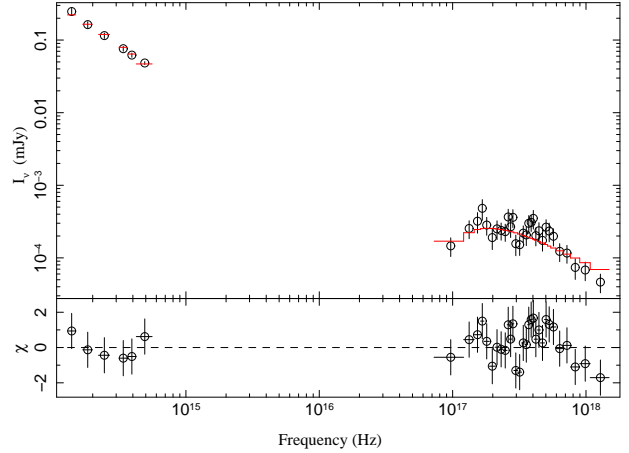


Figure 9. NIR-to-X-ray spectral energy distribution and model for the afterglow at 11 ks after the trigger. The solid red line shows the model. g' -band magnitude is not included in the fit, due to possible contribution from the Ly α transition.

Table 7. Host galaxy parameters from stellar population synthesis modelling

Starburst age (Myr)	~ 250
Extinction (mag)	0.15 ± 0.15
M_B	-22.1 ± 0.2
$\log(M_*/M_\odot)$	$9.9^{+0.2}_{-0.3}$
SFR ($M_\odot \text{ yr}^{-1}$)	40^{+80}_{-25}

pute theoretical magnitudes and compare them to the observed photometry. For the model input, we assume stellar models from Bruzual & Charlot (2003), based on an IMF from Chabrier (2003) and a Calzetti dust attenuation law (Calzetti et al. 2000). Table 7 lists the galaxy parameters resulting from the best-fit to the HAWK-I, NOT and GTC data. The best fit is obtained with a $\chi^2 = 8$ for the 7 data points used in the modelling. Most of the contribution to the χ^2 comes from the B -band observations. This data point lies $\approx 3\sigma$ above the best-fit and the g -band measurement, which probes a very similar wavelength range. The reported value of the SFR takes into account the uncertainty in the dust attenuation, and thus has large error bars. We observe a significant Balmer break, which is well fit with star-burst ages between 50 and 500 Myr. The SFR of $\sim 40 M_\odot \text{ yr}^{-1}$ is consistent with the results from Sect. 3.6.

3.11 Kinematics

The X-shooter spectrum contains information both on the kinematics of the absorbing gas along the line-of-sight to the location of the burst inside the host galaxy, as well as kinematics of the emitting gas in H II regions probed by the emission lines. The emission lines have a full-width-at-half-maximum (FWHM) of around 210 km s^{-1} from a Gaussian fit, see Table 6. This fairly large width is indicative of a galaxy with a large dynamical mass, in agreement with the result in Sect. 3.10. We do not observe rotation in the 2 dimensional spectrum, as the galaxy is likely too small to be rotational supported. The absorption line width measured

as in Ledoux et al. (2006) is 457 km s^{-1} based on the Si II $\lambda 1808$ line. This is consistent with the correlation between absorption line width and metallicity for GRB host galaxies found in Arabsalmani et al. (2014). The velocity for each absorption component, with respect to the emission lines, is given in Table 3. The emission lines are in between in redshift, with the c+d+e component being slightly closer. The different gas components and their geometry is discussed in Sect. 4.5.

3.12 Intervening Systems

We identify two intervening systems along the line of sight. At redshifts $z = 1.959$ we observe the Ly α line, as well as various metal transitions (C IV, Fe II and Mg II). At $z = 1.664$ we detect Mg II, Fe II and a possible Al III absorption. The intervening systems will not be discussed further in this work.

4 DISCUSSION AND IMPLICATIONS

4.1 Abundance Measurements from Absorption and Emission Lines

The metallicity of GRB hosts is usually determined either directly through absorption line measurements, or via the strong-line diagnostics using nebular-line fluxes. The two methods probe different physical regions; the ISM of the host galaxy along the line of sight as opposed to the ionised star-forming H II regions emission-weighted over the whole galaxy. Hence, the two methods are not necessarily expected to yield the same metallicity. Still, we expect the line of sight to probe the gas towards the GRB, and thus absorption-line metallicity should not differ dramatically from the one derived using the emission lines (local measurements from the solar neighbourhood show a concurrence of the two, see e.g., Esteban et al. 2004). Only few cases have previously been reported where measurements were possible using both methods, and none of these include GRB-DLAs (for QSO-DLAs see e.g., Bowen et al. 2005). The challenge is that the redshift has to be high enough ($z \gtrsim 1.5$) to make Ly α observable from the ground, while at the same time the host has to be massively star-forming to produce sufficiently bright emission lines. Furthermore, the strong-line diagnostics are calibrated at low redshifts, with only few high redshift cases available (see for instance Christensen et al. 2012).

On this background, GRB 121024A offers important knowledge needed to compare metallicities of GRBs at different redshifts and possibly extend the calibration of strong-line diagnostics. We find that the three nebular line diagnostics R_{23} , $O3N2$ and $N2$ all agree on an oxygen abundance of $12 + \log(O/H) \sim 8.4$. Expressing this in solar units we get a metallicity of $[O/H] \sim -0.3$ (or slightly lower if we disregard the value found from the R_{23} diagnostic, given that we cannot convincingly distinguish between the upper and lower branch). This is indeed consistent with the absorption line measurement from the low-depletion elements (dust-corrected value) $[Zn/H]_{\text{corr}} = -0.5 \pm 0.2$.

Krogager et al. (2013) found a slightly lower metallicity from absorption lines for the system associated with quasar

Q2222-0946, compared to the emission-line metallicity. However, this is easily explained by the very different regions probed by the nebular lines (6 kpc above the galactic plane for this quasar) and the sight line, see also Péroux et al. (2012). QSO-DLA lines of sight intersect foreground galaxies, while the metallicity probed with GRB-DLAs are from the GRB birthplace in the host galaxy, likely star forming H II regions, hence the two regions are presumably geometrically close. Note though that Noterdaeme et al. (2012) find different values for the metallicities, even with a small impact parameter between QSO and absorber, for QSO-DLAs.

4.2 Molecular Hydrogen in GRB-DLAs

The lack of detection of molecular hydrogen towards GRBs has puzzled astronomers (see e.g. Tumlinson et al. 2007), given that long GRBs are associated with active star formation, and hence are expected to show signatures of molecular clouds. Compared to QSO-DLA line of sights then, we would expect the presence of H₂ to be more common for GRB-DLAs, as the QSO-DLA line of sights have a high probability to intersect the outskirts/halo of the intervening galaxy, where we would anticipate a low molecular content. Recently, a number of H₂ detections in GRB afterglows have been reported (Prochaska et al. 2009; Krühler et al. 2013; D’Elia et al. 2014), making GRB121024A the fourth definite case. This detection supports the emerging picture that dust has played a major role in biasing past observations against molecular detection (e.g. Ledoux et al. 2009). The molecules are thought to form on the surface of dust grains, and once formed, shielded from Lyman-Werner photons by the grains. Krühler et al. (2013) suggest that it is likely this connection that is responsible for the low number of H₂ detections towards GRB-DLAs. The high dust column density makes the GRB afterglow UV-faint, preventing high S/N spectroscopy, which is needed to identify the presence of molecular gas. They illustrate this argument by investigating the metallicity, $N(\text{H I})$ and dust depletion parameter space, showing that the GRB-DLAs with unsuccessful molecular searches fall outside the region where we would expect detections (with the only exception being GRB 050829A). This argument is supported by the observed $\log N(\text{H I})$, metallicity and depletion factor of GRB 121024A, which lie inside this regions for which we expect molecular detections.

The high level of dust depletion observed in this GRB-DLA (see Sect. 3.2), is consistent with molecular detections in QSO-DLAs (Noterdaeme et al. 2008; Krühler et al. 2013), where there is a strong preference for H₂-bearing DLAs to have significant depletion factors. The dependence on the total neutral hydrogen column density is weak (although intrinsically-weak molecular lines are better constrained in strong DLAs), whereas the parameter that seems to determine whether H₂ is detected, is the column density of iron locked into dust. The $\log N(\text{Fe})_{\text{dust}}$ that we measure is 2 dex higher than the column density above which a significant presence of molecules has been observed in QSO-DLAs (Noterdaeme et al. 2008). Indeed De Cia et al. (2013) studied $\log N(\text{Fe})_{\text{dust}}$ and concluded that GRB hosts are promising sites for molecular detections.

D’Elia et al. (2014) find a molecular fraction for GRB 120327A of $\log(f)$ between -7 and -4 with a depletion factor of $[Zn/Fe] = 0.56 \pm 0.14$, while for the dustier line of

sight towards GRB 120815A Krühler et al. (2013) reports a value of $\log(f) = -1.14 \pm 0.15$ ($[\text{Zn}/\text{Fe}] = 1.01 \pm 0.10$). For GRB 121024A we find intermediate values, although with the high noise-level the numbers are consistent with those reported for GRB 120815A (Prochaska et al. 2009, only report limits on both the molecular fraction and the Zn+Fe column densities). Although the sample is too small to infer anything statistically, it appears that the H₂ detection criteria in GRB afterglows follow the trend observed for QSO-DLAs.

4.3 The Mass-Metallicity Relation at $z \sim 2$

Having determined stellar mass, metallicity and SFR of the GRB host, we can investigate whether the galaxy properties are consistent with the mass-metallicity relation at the observed redshift. Appropriate for a redshift of $z \approx 2$, we use equation 5 from Mannucci et al. (2010):

$$12 + \log(\text{O}/\text{H}) = 8.90 + 0.47 \times (\mu_{0.32} - 10)$$

where $\mu_{0.32} = \log(M_* [M_\odot]) - 0.32 \times \log(\text{SFR}_{\text{H}\alpha} [M_\odot] \text{yr}^{-1})$. Using the stellar mass from Sect. 3.10 and the SFR from H α we find an equivalent metallicity of $12 + \log(\text{O}/\text{H}) = 8.6 \pm 0.2$ ($[\text{O}/\text{H}] = -0.1 \pm 0.2$). The error does not include a contribution from the scatter in the relation, and is hence likely underestimated. This value is consistent with our metallicity determinations. This supports the points made above, and throughout this paper, that the host of GRB 121024A is a fairly typical star-forming galaxy. This makes GRBs a powerful tool to study the conditions required for star formation at high redshifts.

4.4 Grey Dust Extinction?

We determine the dust extinction/attenuation of the host galaxy of GRB 121024A both from the Balmer decrement (Sect. 3.8) and a fit to the X-ray and optical spectral energy distribution (SED, see Sect. 3.9), as well as from the stellar population synthesis modelling (Sect. 3.10). The first method determines the attenuation of the host H II regions (from the X-shooter spectrum alone), while the SED fitting probes the extinction along the line of sight (using XRT+GROND data). The stellar population synthesis modelling models the host attenuation as a whole (using host photometry). All methods determine the amount of extinction/attenuation by comparing different parts of the spectrum with known/inferred intrinsic ratio, and attribute the observed change in spectral form to dust absorption and scattering. We find values that agree on a colour index $E(B - V) \sim 0.04$ mag. This value is small, but falls within the range observed for DLA systems. However, these are the low metallicity part of the DLA sample. For our case we would expect a much higher amount of reddening at our determined H I column density and metallicity. Using the metallicity of $[\text{Zn}/\text{H}]_{\text{corr}} = -0.5$, column density $\log N(\text{H I}) = 21.80$, dust-to-metal ratio $\mathcal{DTM} = 0.8\text{--}1.0$ (see Sect. 3.2), and a reference Galactic dust-to-metal ratio $A_{V,\text{Gal}}/N_{(\text{H},\text{Gal})} = 0.45 \times 10^{-21}$ mag cm² (Watson 2011), we expect an extinction of the order $A_V \sim 0.7 - 0.9$ mag. This is clearly incompatible with the determined reddening, as it would require $R_v > 15$ (R_V for the Galaxy is

broadly in the range 2–5). For the Balmer decrement and SED fitting we have examined different extinction curves (MW and LMC besides the SMC) and we have tried fitting the SED with a cooling break, neither option changing the extinction significantly. In an attempt to drive up the fitted reddening, we tried fitting the SED with a lower Galactic $N(\text{H I})$ and reddening. While keeping reasonable values (it is unphysical to expect no Galactic extinction at all), and fitting with the break, the resulting highest colour index is $E(B - V) \sim 0.06$ mag. This is still not compatible with the metallicity-derived value, so this difference needs to be explained physically.

One possibility to consider is that the host could have a lower dust-to-metals ratio, and hence we overestimate the extinction we expect from the metallicity. We see no sign of this from the depletion pattern though, in fact we observe quite a high level of depletion, while the metallicity is fairly typical for a GRB-DLA (and fits the mass-metallicity relation). In addition we observe a relatively high amount of molecular hydrogen, which we argue is possible because of the high dust column. Another possibility then, is an unconventional extinction curve for this GRB-DLA. If the dust extinction is 'grey', i.e., has a much weaker dependence on wavelength than in the local extinction laws (corresponding to a large R_V , physically interpreted as a larger grain size), then a given visual extinction will be much less apparent in the SED and thus underestimated in our analysis. Gao, Jiang & Li (2008) claim a grey extinction law for GRB lines of sight determined by comparing observed spectra to intrinsic ones (by extrapolating from X-rays), arguing for grain growth through coagulation in the dense molecular clouds surrounding GRBs. The larger grains have an extinction that is less dependent on wavelength. Preferably destruction of the smaller grains by the GRB would be another possibility, but is unlikely in our case, as the gas probed is shown to be far from the GRB sight ('c+d+e' component). We note that the other GRB-DLAs with molecular hydrogen detected show an expected amount of reddening (using a standard extinction curve), though anomalies are not uncommon in GRB observations, see for instance Perley et al. (2008).

Given the large difference between the SED and metallicity-derived value, the resulting extinction law for our GRB-DLA would be very extreme, so we consider the extinction problem to be unsolved.

4.5 Cold Molecular Gas and Excited Gas

One of the striking features of the metal absorption-line profiles observed towards GRB 121024A is that they consist of two widely separated groups of velocity components (a+b and c+d+e, see Sect. 3.1). The separation is of about 400 km s⁻¹, which lies at the high end of the velocity distribution of Møller et al. (2013) and Ledoux et al. (2006). This suggests that either the two components belong to separate galaxies, or that this galaxy is fairly massive compared to the average GRB host of $\sim 10^9 M_\odot$ (Savaglio et al. 2009; Castro Cerón et al. 2010, but see also Perley et al. 2013 and Hunt et al. 2014). The scenario with separate galaxies is disfavoured, because the two absorption components show very similar relative abundances (see Table 3) and also because the emission lines are centred in between the two absorption

components (and are broad, see Sect. 3.11). Thus, a likely possibility is that the two absorption components are probing different regions within the host. This is in agreement with the mass found in Sect. 3.10, of almost $10^{10} M_{\odot}$.

Furthermore, the blue (a+b) and the red (c+d+e) absorption components are associated with gas at very different physical conditions. On one hand, Fe II, Ni II and Si II fine-structure lines are detected only in the blue component. These lines are excited by the GRB radiation at a distance of ~ 700 pc. On the other hand, H₂ molecules are detected in the red component only, indicating a gas that is colder and not disturbed by the GRB (at a distance of minimum 3.5 kpc), and likely in the form of diffuse molecular gas.

Comparing with the systemic redshift from the emission lines, it appears that the excited gas closest to the GRB is moving towards us (at about 225 km s^{-1} compared to the whole system as probed by emission), while the colder gas closer to us (further from the GRB) is moving away (a velocity of about -100 km s^{-1}). Disregarding transverse motion the gas clouds seem to be moving towards each other. Because of the similar metallicity of the two clouds, we assume they both belong to the same system. A possible scenario then, is that we are observing towards a galactic fountain with in-falling clouds, although a distance between the gas clouds of > 3 kpc is at the high end of what is observed for galactic fountains (see for instance Melioli et al. 2008; Wakker et al. 2008).

While the current spectral resolution does not allow a more detailed study, this work shows how powerful the observation of GRBs can be to start dissecting individual building-block components of star-forming galaxies at $z \sim 2$ and above.

ACKNOWLEDGMENTS

MF acknowledges support from the University of Iceland Research fund. ADC acknowledges support by the Weizmann Institute of Science Dean of Physics Fellowship and the Koshland Center for Basic Research. The Dark Cosmology Centre is funded by the DNRF. RLCS is supported by a Royal Society Dorothy Hodgkin Fellowship. JPUF acknowledges support from the ERC-StG grant EGG-278202. CCT is supported by a Ramón y Cajal fellowship and acknowledges partial support by project AYA2012-39362-C02-02. The research activity of Ad.U.P. and J.G. is supported by Spanish research project AYA2012-39362-02-02. Ad.U.P. acknowledges support by the European Commission under the Marie Curie Career Integration Grant programme (FP7-PEOPLE-2012-CIG 322307). SS acknowledges support from CONICYT-Chile FONDECYT 3140534, Basal-CATA PFB-06/2007, and Project IC120009 "Millennium Institute of Astrophysics (MAS)" of Iniciativa Científica Milenio del Ministerio de Economía, Fomento y Turismo. We thank Alain Smette for providing the telluric spectrum, and the referee for very constructive feedback.

REFERENCES

Arabsalmani M. et al., 2014, MNRAS, submitted

- Asplund M., Grevesse N., Sauval A. J., Scott P., 2009, ARA&A, 47, 481
- Barthelmy S.D. et al., 2005, SSRv, 120, 143
- Bowen D. V., Jenkins E. B., Pettini M., Tripp T. M., 2005, ApJ, 635, 880
- Bruzual G., Charlot S., 2003, MNRAS, 344, 1000
- Calzetti D., Armus L., Bohlin R. C., Kinney A. L., Koornneef J., Storchi-Bergmann T., 2000, ApJ, 533, 682
- Cano Z., 2013, MNRAS, 434, 1098
- Castro Cerón J. M. et al., 2010, ApJ, 721, 1919
- Cepa J. et al., 2000, SPIE, 4008, 623
- Chabrier G., 2003, PASP, 115, 763
- Christensen L. et al., 2012, MNRAS, 427, 1973
- De Cia A. et al., 2012, A&A, 545, 64
- De Cia A., Ledoux C., Savaglio S., Schady P., Vreeswijk P. M., 2013, A&A, 560, 88
- D'Elia V. et al., 2014, A&A, 564, 38
- Elíasdóttir Á. et al., 2009, ApJ, 697, 1725
- Draine B. T., 2000, ApJ, 532, 273
- Draine B. T., Hao L., 2002, ApJ, 569, 780
- Esteban C., Peimbert M., García-Rojas J., Ruiz M. T., Peimbert A., Rodríguez M., 2004, MNRAS, 355, 229
- Fynbo J. P. U. et al., 2009, ApJS, 185, 526
- Fynbo J. P. U. et al., 2011, MNRAS, 413, 2481
- Fynbo J. P. U. et al., 2013, MNRAS, 436, 361
- Gehrels N. et al., 2004, ApJ, 611, 1005
- Goldoni P., Royer F., François P., Horrobin M., Blanc G., Vernet J., Modigliani A., Larsen J., 2006, in SPIE conf. ser., 6269
- Greiner J. et al., 2007, The Messenger, 130, 12
- Greiner J. et al., 2008, PASP, 120, 405
- Haehnelt M. G., Steinmetz M., Rauch M., 1998, ApJ, 495, 647
- Hjorth J. et al., 2003, Nature, 423, 847
- Houck J. C., Denicola L.A., 2000, ASPC, 216, 519
- Hunt L. K. et al., 2014, A&A, 565, 112
- Jakobsson P. et al., 2006, A&A, 460, L13
- Jenkins E. B., 2009, ApJ, 700, 1299
- Jorgesen R., Wolfe A. M., 2014, ApJ, 785, 16
- Kennicutt Jr. R. C., 1998, ARA&A, 36, 189
- Kewley L. J., Ellison S. L., 2008, ApJ, 681, 1183
- Krogager. J.-K. et al., 2013, MNRAS, 433, 3091
- Krühler T. et al., 2008, ApJ, 685, 376
- Krühler T. et al., 2012, A&A, 546, 8
- Krühler T. et al., 2013, A&A, 557, 18
- Kudritzki et al., 2012, ApJ, 747, 15
- Levesque E. M., Berger E., Kewley L. J., Bagley M. M., 2010, AJ, 139, 694
- Ledoux C., Petitjean P., Bergeron J., Wampler E. J., Srianand R., 1998, A&A, 337, 51
- Ledoux C., Bergeron J., Petitjean P., 2002a, A&A, 385, 802
- Ledoux C., Srianand R., Petitjean P., 2002b, A&A, 392, 781
- Ledoux C., Petitjean P., Srianand R., 2003, MNRAS, 346, 209
- Ledoux C., Petitjean P., Fynbo J. P. U., Møller P., Srianand R., 2006, A&A, 457, 71
- Ledoux C., Vreeswijk P. M., Smette A., Fox A. J., Petitjean P., Ellison S. L., Fynbo J. P. U., Savaglio S., 2009, A&A, 506, 661
- Gao J., Jiang B. W., Li A., 2008, ApJ, 707, 89

- Lodders K., Palme H., Gail H. P., 2009, *Landolt Börnstein*, 44
- Mannuci F., Cresci G., Maiolino R., Marconi A., Gnerucci A., 2010, *MNRAS*, 408, 2115
- Mattsson L., De Cia A., Andersen A.C., Zafar T., 2014, *MNRAS*, 440, 1562
- McGaugh S. S., 1991, *ApJ*, 380, 140
- Melioli C., Brighenti F., D’Ercole A., De Gouveia Dal Pino E. M., 2008, *MNRAS*, 388, 573
- Morton D. C., 2003, *ApJs*, 149, 205
- Møller P., 2000, *The Messenger*, 99, 31
- Møller P., Fynbo J. P. U., Ledoux C., Nilsson K. K., 2013, *MNRAS*, 430, 2680
- Noterdaeme P., Ledoux C., Petitjean P., Srianand R., 2008, *A&A*, 481, 327
- Noterdaeme P. et al., 2012, *A&A*, 540, 63
- Osterbrock D. E., 1989, *Astrophysics of Planetary Nebulae and Active Galactic Nuclei* (University Science Books)
- Pei Y. C., 1992, *ApJ*, 395, 130
- Perley D. A., 2008, *ApJ*, 672, 449
- Perley D. A., 2013, *ApJ*, 778, 128
- Péroux C., Bouché N., Kulkarni V. P., York D. G., Vladilo G., 2012, *MNRAS*, 419, 3060
- Pettini M., Pagel B. E. J., 2004, *MNRAS*, 348, L59
- Pettini M., Smith L. J., Hunstead, R. W., King D. L., 1994, *ApJ*, 426, 79
- Prochaska J. X., Wolfe A. M., 1997, *ApJ*, 487, 73
- Prochaska J. X., Chen H. W., Bloom J. S., 2006, *ApJ*, 648, 95
- Prochaska J. X., Chen H. W., Dessauges-Zavadsky M., Bloom J. S., 2007, *ApJ*, 666, 267
- Prochaska J. X. et al., 2009, *ApJ*, 691, L27
- Reichert D., 2005, *Nuovo Cimento C Geophysics Space Physics C*, 28, 767
- Savage B. D., Sembach K., R., 1996, *ARA&A*, 34, 279
- Savaglio S., 2001, *IAUS*, 204, 307
- Savaglio S., Glazebrook K., Le Borgne D., 2009, *ApJ*, 691, 182
- Schlegel D. J., Finkbeiner D. P., Davis M., 1998, *ApJ*, 500, 525
- Schulze S. et al., 2014, *A&A*, 566, 102
- Sheffer Y., Prochaska J. X., Draine B. T., Perley D. A., Bloom J. S., 2009, *ApJ*, 701, 63
- Smette A., Sana H., Horst H., 2010, *Highlights of Astronomy*, 15, 533
- Smith et al., 2002, *AJ*, 123, 2121
- Sparre M. et al., 2011, *ApJ*, 735, L24
- Sparre M. et al., 2014, *ApJ*, 785, 105
- Stanek K. Z. et al., 2003, *ApJ*, 591, L17
- Starling R. L. C., Wijers R. A. M. J., Wiersema K., Rol E., Curran P. A., Kouveliotou C., van der Horst A. J., Heemskerk M. H. M., 2007, *ApJ*, 661, 787
- Steeghs D., McClintock J. E., Parsons S. G., Reid M. J., Littlefair S., Dhillon V. S., 2013, *ApJ*, 768, 185
- Tody D., 1997, *Astronomical Society of the Pacific Conference Series*, 125, 451
- Treyer M. et al., 2007, *ApJs*, 173, 256
- Tumlinson J., Prochaska J. X., Chen H. W., Dessauges-Zavadsky M., Bloom J. S., 2007, *ApJ*, 668, 667
- Vernet J. et al., 2011, *A&A*, 536, A105
- Vladilo G., Centurión M., Levshakov S. A., Péroux C., Khare P., Kulkarni V. P., York D. G., 2006, *A&A*, 454, 151
- Vreeswijk P. M. et al., 2004, *A&A*, 419, 927
- Vreeswijk P. M. et al., 2007, *A&A*, 468, 83
- Vreeswijk P. M. et al., 2013, *A&A*, 549, 22
- Wakker B. P., York D. G., Wilhelm R., Barentine J. C., Richter P., Beers T. C., Ivezić Ž, Howk J. C., 2008, *ApJ*, 672, 298
- Watson D., 2011, *A&A*, 533, 16
- Wiersema K. et al., 2007, *A&A*, 464, 529
- Wiersema K. et al., 2014, *Nature*, 509, 201
- Willingale R., Starling R. L. C., Beardmore A. P., Tanvir N. R., O’Brien P. T., 2013, *MNRAS*, 431, 394
- Wilms J., Allen A., McCray R., 2000, *ApJ*, 542, 914
- Wolfe A. M., Gawiser E., Prochaska J. X., 2005, *ARAA*, 43, 861
- Zafar T., Watson D., 2013, *A&A*, 560, 26

APPENDIX A: SKYNET MAGNITUDE TABLES

Tables A1, A2, A3, A4, A5 and A6 give the magnitudes used for the optical light-curve input to model the distance between the excited gas (component a+b) and the burst itself.

Table A1. Skynet - Filter *R*

Filter	Time (h)	Exposure time	S/N	Mag. (Vega)
<i>R</i>	0.01656	1 × 10s	27.7	15.01 ± 0.04
<i>R</i>	0.02232	1 × 10s	18.9	15.51 ± 0.06
<i>R</i>	0.02760	1 × 10s	12.1	15.88 ± 0.09
<i>R</i>	0.03288	1 × 10s	7.58	16.0 ^{+0.2} _{-0.1}
<i>R</i>	0.04032	1 × 20s	10.7	16.3 ± 0.1
<i>R</i>	0.04824	1 × 20s	9.35	16.4 ± 0.1
<i>R</i>	0.06720	1 × 40s	7.45	16.5 ^{+0.2} _{-0.1}
<i>R</i>	0.08088	1 × 40s	13.1	16.68 ^{+0.09} _{-0.08}
<i>R</i>	0.10824	1 × 40s	5.47	16.9 ± 0.2
<i>R</i>	0.18216	1 × 80s	5.82	17.5 ± 0.2
<i>R</i>	0.20880	1 × 80s	3.58	17.0 ± 0.3
<i>R</i>	0.24744	1 × 160s	10.9	17.4 ± 0.1
<i>R</i>	0.35520	1 × 160s	5.37	17.8 ± 0.2
<i>R</i>	0.40536	1 × 160s	6.08	17.6 ± 0.2
<i>R</i>	0.50928	1 × 160s	2.86	17.9 ^{+0.4} _{-0.3}
<i>R</i>	0.55584	1 × 160s	6.08	17.5 ± 0.2
<i>R</i>	0.66000	1 × 160s	5.53	17.6 ± 0.2
<i>R</i>	0.91992	3 × 160s	5.79	18.4 ± 0.2
<i>R</i>	1.28712	4 × 160s	6.64	18.79 ± 0.2
<i>R</i>	1.84008	9 × 160s	3.68	19.3 ± 0.3
<i>R</i>	2.79768	7 × 160s	6.72	19.5 ^{+0.2} _{-0.1}
<i>R</i>	3.21240	7 × 160s	8.31	19.8 ± 0.1
<i>R</i>	3.59184	7 × 160s	10.1	19.8 ± 0.1
<i>R</i>	4.12824	12 × 160s	10.7	19.8 ± 0.1
<i>R</i>	4.9908	18 × 160s	7.18	20.0 ± 0.1
<i>R</i>	24.5124	40 × 160s	1.94	21.9 ^{+0.7} _{-0.4}

Table A2. Skynet - Filter *B*

Filter	Time (h)	Exposure time	S/N	Mag. (Vega)
<i>B</i>	0.02520	2 × 10s	4.98	17.2 ± 0.2
<i>B</i>	0.05592	2 × 20s	4.22	17.9 ^{+0.3} _{-0.2}
<i>B</i>	0.12144	3 × 40s	5.10	18.3 ± 0.2
<i>B</i>	0.27456	2 × 160s	5.61	18.8 ± 0.2
<i>B</i>	3.87000	37 × 160s	5.96	21.2 ± 0.2

Table A3. Skynet - Filter *I*

Filter	Time (h)	Exposure time	S/N	Mag. (Vega)
<i>I</i>	0.02328	1 × 5s	13.4	14.88 ± 0.08
<i>I</i>	0.02784	1 × 5s	9.57	15.1 ± 0.1
<i>I</i>	0.03312	1 × 10s	10.2	15.4 ± 0.1
<i>I</i>	0.04032	1 × 20s	14.6	15.49 ^{+0.08} _{-0.07}
<i>I</i>	0.04896	1 × 20s	11.8	15.70 ^{+0.1} _{-0.09}
<i>I</i>	0.05616	1 × 10s	2.34	16.2 ^{+0.5} _{-0.4}
<i>I</i>	0.06672	1 × 40s	5.75	16.2 ± 0.2
<i>I</i>	0.08088	1 × 40s	15.4	16.03 ± 0.07
<i>I</i>	0.09504	1 × 40s	7.74	15.9 ± 0.1
<i>I</i>	0.10896	1 × 40s	7.16	16.2 ^{+0.2} _{-0.1}
<i>I</i>	0.12864	1 × 80s	15.1	16.21 ± 0.07
<i>I</i>	0.15504	1 × 80s	3.84	16.3 ^{+0.3} _{-0.2}
<i>I</i>	0.18216	1 × 80s	9.82	16.5 ± 0.1
<i>I</i>	0.20880	1 × 80s	5.14	16.7 ± 0.2
<i>I</i>	0.24744	1 × 160s	16.3	16.72 ± 0.07
<i>I</i>	0.30144	1 × 160s	13.3	16.74 ^{+0.09} _{-0.08}
<i>I</i>	0.35520	1 × 160s	11.3	16.73 ^{+0.1} _{-0.09}
<i>I</i>	0.40536	1 × 160s	6.89	17.0 ^{+0.2} _{-0.1}
<i>I</i>	0.50928	1 × 160s	8.51	16.9 ± 0.1
<i>I</i>	0.55632	1 × 160s	7.10	17.1 ^{+0.2} _{-0.1}
<i>I</i>	0.61248	1 × 160s	6.87	16.8 ^{+0.2} _{-0.1}
<i>I</i>	0.66000	1 × 160s	5.78	17.2 ± 0.2
<i>I</i>	0.71592	1 × 160s	3.53	17.3 ± 0.3
<i>I</i>	0.81528	2 × 160s	5.50	17.4 ± 0.2
<i>I</i>	0.94704	2 × 160s	11.4	17.45 ^{+0.1} _{-0.09}
<i>I</i>	1.21368	1 × 160s	5.87	17.7 ± 0.2
<i>I</i>	1.33872	2 × 160s	6.90	18.1 ^{+0.2} _{-0.1}
<i>I</i>	1.53672	2 × 160s	3.92	18.3 ^{+0.3} _{-0.2}
<i>I</i>	1.75560	1 × 160s	2.80	18.0 ^{+0.4} _{-0.3}
<i>I</i>	2.07528	5 × 160s	4.51	18.4 ^{+0.3} _{-0.2}
<i>I</i>	2.46480	5 × 160s	3.76	18.6 ± 0.3
<i>I</i>	2.83080	6 × 160s	8.36	18.64 ± 0.1
<i>I</i>	3.21504	7 × 160s	12.1	18.72 ± 0.09
<i>I</i>	3.59496	7 × 160s	13.7	18.71 ± 0.08
<i>I</i>	4.10328	11 × 160s	12.8	18.99 ^{+0.09} _{-0.08}
<i>I</i>	4.81200	12 × 160s	9.54	193 ± 0.1
<i>I</i>	5.63112	16 × 160s	6.02	19.2 ± 0.2
<i>I</i>	24.3192	47 × 160s	1.89	21 ^{+0.7} _{-0.4}

Table A4. Skynet - Filter *g'*

Filter	Time (h)	Exposure time	S/N	Mag. (Vega)
<i>g'</i>	0.03312	1 × 20s	3.76	17.4 ± 0.3
<i>g'</i>	0.25032	1 × 80s	4.45	18.3 ^{+0.3} _{-0.2}
<i>g'</i>	0.69912	1 × 80s	2.16	19.5 ^{0.6} _{-0.4}

Table A5. Skynet - Filter *r'*

Filter	Time (h)	Exposure time	S/N	Mag. (Vega)
<i>r'</i>	0.05688	1 × 20s	6.15	16.9 ± 0.2
<i>r'</i>	0.15576	1 × 80s	10.6	17.4 ± 0.1
<i>r'</i>	0.30168	1 × 160s	11.8	17.66 ^{+0.1} _{-0.09}
<i>r'</i>	0.50952	1 × 160s	8.21	18.0 ± 0.1
<i>r'</i>	0.56088	1 × 80s	5.14	18.0 ± 0.2

Table A6. Skynet - Filter *i'*

Filter	Time (h)	Exposure time	S/N	Mag. (Vega)
<i>i'</i>	0.08088	1 × 20s	5.22	16.3 ± 0.2
<i>i'</i>	0.35328	1 × 80s	4.50	17.6 ^{+0.3} _{-0.2}
<i>i'</i>	0.61272	1 × 160s	4.91	17.9 ± 0.2
<i>i'</i>	0.66408	1 × 80s	3.06	17.9 ^{+0.4} _{-0.3}
<i>i'</i>	21.99288	38 × 160s	1.13	20.9 ^{+1.2} _{-0.6}